Virology 431 (2012) 58–70

Contents lists available at SciVerse ScienceDirect

Virology

journal homepage: www.elsevier.com/locate/yviro

Ultrastructural study of Rift Valley fever virus in the mouse model

Christopher Reed, Keith E. Steele [1], Anna Honko, Joshua Shamblin, Lisa E. Hensley [2], Darci R. Smith *

United States Army Medical Research Institute of Infectious Diseases (USAMRIID), Fort Detrick, MD, United States

ARTICLE INFO

Article history:
Received 30 March 2012
Returned to author for revisions
23 April 2012
Accepted 20 May 2012
Available online 9 June 2012

Keywords:
Rift Valley fever
Viral hemorrhagic fever
Electron microscopy
Pathogenesis
Ultrastructure
Mouse model

ABSTRACT

Detailed ultrastructural studies of Rift Valley fever virus (RVFV) in the mouse model are needed to develop and characterize a small animal model of RVF for the evaluation of potential vaccines and therapeutics. In this study, the ultrastructural features of RVFV infection in the mouse model were analyzed. The main changes in the liver included the presence of viral particles in hepatocytes and hepatic stem cells accompanied by hepatocyte apoptosis. However, viral particles were observed rarely in the liver; in contrast, particles were extremely abundant in the CNS. Despite extensive lymphocytolysis, direct evidence of viral replication was not observed in the lymphoid tissue. These results correlate with the acute-onset hepatitis and delayed-onset encephalitis that are dominant features of severe human RVF, but suggest that host immune-mediated mechanisms contribute significantly to pathology. The results of this study expand our knowledge of RVFV–host interactions and further characterize the mouse model of RVF.

Published by Elsevier Inc.

Introduction

Rift Valley fever virus (RVFV) is a negative sense, single-stranded RNA virus in the genus *Phlebovirus* (family *Bunyaviridae*). The virus was first isolated in 1930 in East Africa (Daubney, 1931) and has since caused severe epizootics throughout Africa and the Arabian peninsula. Human cases have been reported in much of Africa, Saudi Arabia, and Yemen with recent outbreaks in Kenya during 2006–2007 (Bird et al., 2009). Severe outbreaks have involved tens of thousands of both human and livestock cases for which no effective licensed vaccine or antiviral drug is available. Additionally, RVFV is easily aerosolized (Abu-Elyazeed et al., 1996), which causes concern for its use as a potential biological weapon (Sidwell and Smee, 2003). Therefore, RVFV has been identified as a category A, or high-priority agent, by the National Institute for Allergy and Infectious Diseases (NIAID); is on the Center for Disease Control and Prevention's (CDC) bioterrorism agent list; and is classified as a Department of Health and Human Services (HHS) and United States Department of Agriculture (USDA) overlap select agent.

RVFV is an arthropod-borne virus (arbovirus) that causes abortion and high mortality in domestic livestock. Humans become infected during the course of epizootics (Meegan, 1989) either by mosquito bite, or by contact with tissues, blood, or other fluids of infected animals. Following an incubation period of 2–6 days, an abrupt onset of fever, chills, and general malaise typically ensues. In most cases, the human disease is mild, and recovery occurs without major consequences. However, in severe cases (which affect around 1–3% of infected individuals), acute-onset liver disease, delayed onset encephalitis, retinitis, blindness, or a hemorrhagic syndrome may occur, with a case fatality rate of 10–20% in hospitalized individuals (Laughlin et al., 1979; Madani et al., 2003; McIntosh et al., 1980).

Several animal models of RVFV infection have been described. Recently, we completed a detailed study to characterize the pathogenesis of RVFV in the BALB/c mouse model (Smith et al., 2010), which showed important similarities to severe human infections. Infection of BALB/c mice with RVFV subcutaneously resulted in high-titer viremia and demonstrated RVFV tropism for a variety of tissue and individual cell types on the bases of histopathology and immunohistochemistry (IHC). A major consequence of infection was overwhelming infection of hepatocytes that subsequently underwent apoptosis. Most mice succumbed to RVFV between days 3 and 6 post-infection (PI) which we attributed primarily to severe hepatitis as indicated by the overwhelming infection of hepatocytes and increase in high levels of hepatic enzymes in the blood. The remaining mice were able to effectively clear virus from the liver and blood, but exhibited neuroinvasion and developed lethal panencephalitis (Smith et al., 2010).

In this report, we extend our investigations of RVFV–host interactions to include the ultrastructural aspects of viral replication, dissemination, and histopathology in the mouse model. Significant ultrastructural changes and viral replication were observed in the liver and the CNS, consistent with the histopathological and

* Corresponding author. Fax: +1 301 619 2290.
E-mail address: darci.smith1@us.army.mil (D.R. Smith).
[1] Present address: MedImmune Inc., One MedImmune Way, Gaithersburg, MD 20878, United States.
[2] Present address: U.S. Food and Drug Administration, 10903 New Hampshire Ave., White Oak Building 31 Room 4128, Silver Spring, MD 20993, United States.

0042-6822/$ - see front matter Published by Elsevier Inc.
http://dx.doi.org/10.1016/j.virol.2012.05.012

immunohistochemical findings previously reported (Smith et al., 2010). Interestingly, viral particles were rarely observed in the liver despite the overwhelming infection of hepatocytes portrayed by IHC in the previous study. In contrast to the liver, abundant viral particles were frequently observed in multiple cell types of the CNS during late time points. Direct evidence of viral replication was not observed in the lymphoid tissue despite widespread apoptosis of lymphocytes. Overall, these findings are consistent with the acute-onset hepatitis and delayed-onset encephalitis that are dominant features of severe human RVF, but inflammation and lack of viral reproduction in hepatocytes as observed in this ultrastructural analysis suggest a critical role of a host immune-mediated mechanism for liver disease. Accordingly, this study further defines the critical pathogenetic processes relevant to human infection and further establishes the basic pathogenesis of RVFV in the mouse model.

Results

Ultrastructural analysis of RVFV-infected mouse tissue specimens revealed evidence of viral infection and replication in multiple cell types. These findings were accompanied by electron microscopic observation of mononuclear and polymorphonuclear white blood cell infiltration and apoptosis in the affected tissues. Importantly, there was early and severe hepatitis with evidence of viral infection of multiple liver cell types and hepatocytic cell death. Animals sampled from later groups that survived this initial phase revealed viral particle budding in multiple cell types of the CNS 5 day PI, which is consistent with the neurological symptoms seen in these mice and previously described. Other noteworthy ultrastructural lesions observed throughout the course of infection included overwhelming lymphocytolysis via apoptosis of classical morphology in the secondary lymphoid tissues, and the appearance of intranuclear inclusion bodies that likely represent viral protein aggregates in multiple cell types and tissues (Yadani et al., 1999). In accordance with previously published in vitro studies of RVF ultrastructure, RVFV particles were observed to be 90–110 nm, roughly spherical, electron-dense viral particles that budded and accumulated in Golgi apparatus cisternae and the endoplasmic reticulum (ER) of susceptible cells (Ellis et al., 1988).

Ultrastructural changes in the liver

Similar to previously described features of RVFV in animal models, livestock, and human cases, the greatest pathological changes associated with infection in the mice of this study were observed in the liver. In particular, hepatocytes and hepatic stellate cells (HSC; also known as perisinusoidal cells) were infected and degenerate (Abdel-Wahab et al., 1978; Morrill et al., 1990). In this study, while samples collected 1 day PI appeared normal, EM examination identified ultrastructural changes as early as 2 day PI. Liver specimens from this time-point revealed expansion of

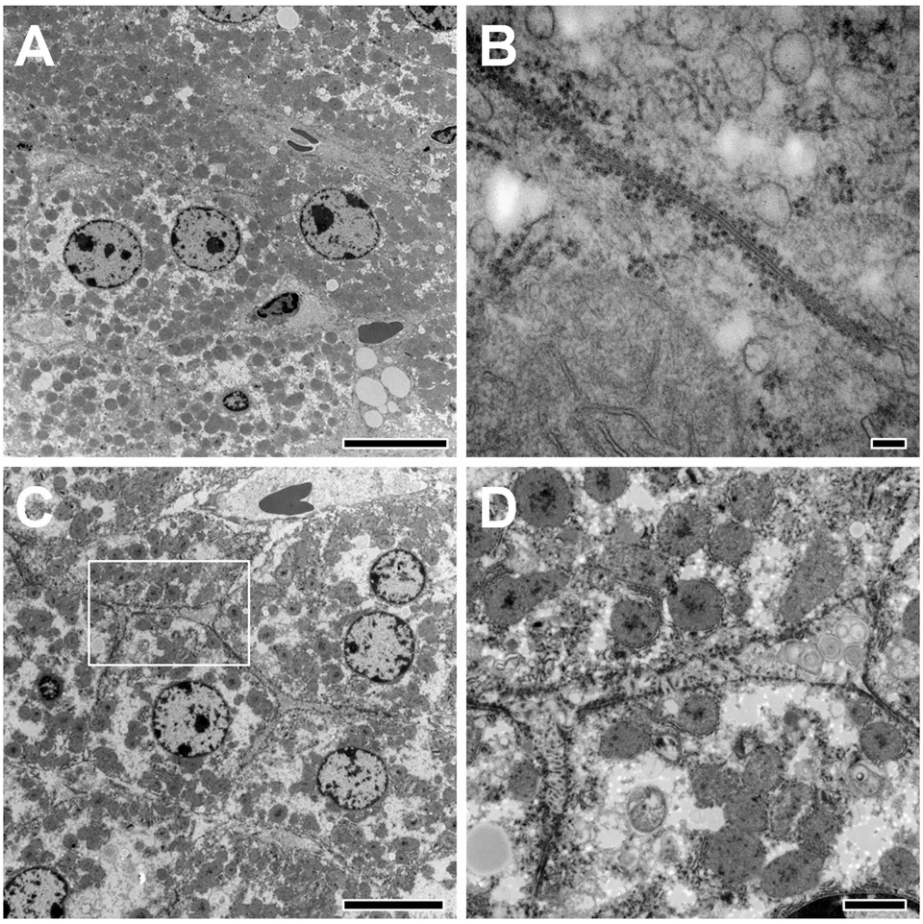

Fig. 1. Liver ultrastructure appeared normal 1 day PI, but loss of interhepatocytic cell junctions led to cell individualization 2 day PI. (A) Low magnification images of liver tissue from an animal sampled 1 day PI. Sinusoidal organization and higher structure appear normal, and fine structure of a hepatocyte gap junction also appears unchanged. (B) Normal gap junction between two hepatocytes 1 day PI. (C) Low magnification image showing interhepatocytic space expansion and individualization 2 day PI. This appears to result from dissolution or restructuring of lateral junctional complexes responsible for maintaining interhepatocytic adhesion. (D) Higher magnification image showing details of the field indicated in (C). Bars: A and C=10 μm, B=100 nm, D=2 μm.

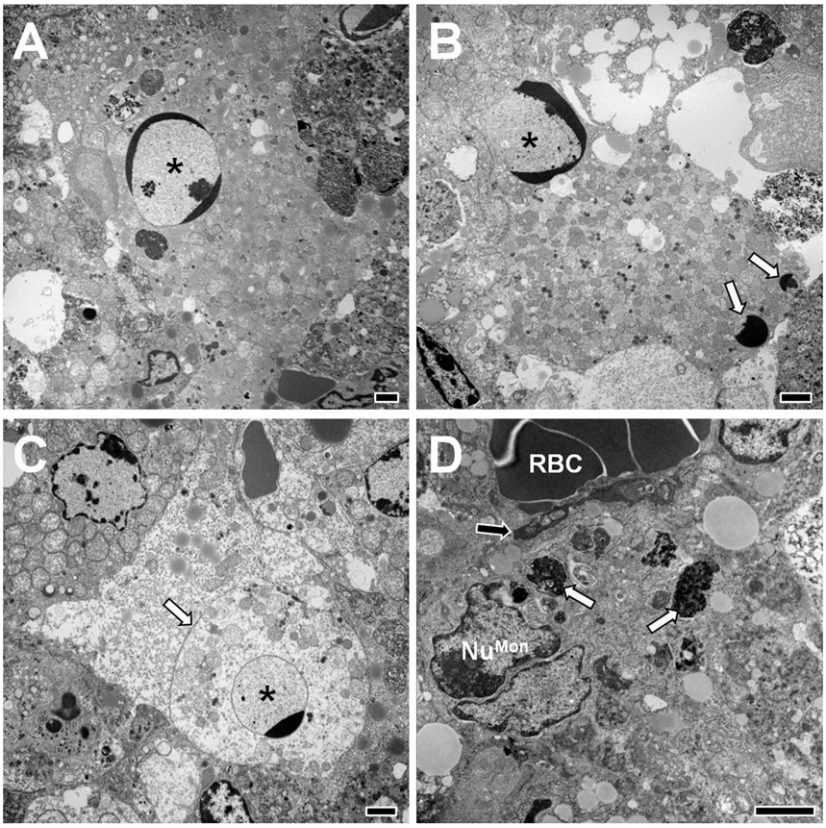

Fig. 2. Most hepatocytes sampled showed signs of apoptosis and mononuclear phagocytes were frequently observed in perisinusoidal and interhepatocellular spaces 3 day PI. (A) Hepatocyte shows highly condensed euchromatin confined to the periphery of the nuclear envelope (pyknosis), seen here in a prototypical crescent-shaped configuration. (B) Hepatocyte, presumably from a later stage of apoptosis, shows both chromatin condensation and fractionation of the nucleus (karyohexis). Nuclear fragments are indicated by white arrows. (C) Hepatocyte from a final stage of apoptosis shows a nearly entirely electron-lucent, contacted cytoplasm. Plasma membrane (indicated by white arrow) has fallen away from neighboring hepatocyte. Asterisks indicate nuclei in each image. (D) A large mononuclear white blood cell with a bilobular nucleus (Nu^{Mon}) is observed in the perisinusoidal space between hepatocytes and sinusoidal endothelium (black arrow). Phagolysosomes filled with necrotic debris (white arrows) are numerous and found throughout the cell's cytoplasm. All bars=2 μm.

interhepatocellular space and loss of lateral junction complexes (Fig. 1). No other pathological changes were identified 2 day PI or earlier.

Widespread apoptosis of hepatocytes first became evident 3 day PI. This was accompanied by mononuclear and polymorphonuclear white blood cell infiltration of the parenchyma, and the hepatic architecture was largely obliterated. Most hepatocytes sampled from both animals at this time-point showed hallmark signs of apoptosis, including cell shrinkage and rounding accompanied by pyknosis and/or karyorrhexis (Fig. 2). Many extrasinusoidal small lymphocytes had colocalized with apoptotic hepatocytes. Rare hepatocytes that maintained their viability through day 4 PI amassed cytoplasmic lipid droplets occluding most normal structures; a lesion corresponding to vacuolar degeneration via conventional histological examination (Fig. 3). Even as liver regeneration was apparent on day 5 PI, this aberrant lipid deposition was observed as late as day 8 PI. The only exceptions to the catastrophic loss of structure were bile duct epithelial cells, which remained intact and apparently uninfected throughout the entire course of infection. Electron-dense, 90–110 nm particles consistent with RVF virions were observed in the lumen of the Golgi apparatus of hepatocytes and HSCs on days 3 and 4 PI (Fig. 4), although this finding was rare, which is in contrast to the significant amount of antigen observed by immunohistochemistry. RVFV particles were often found to share an additional, interior lipid membrane within the Golgi lumen that was separate and distinct from the Golgi's membrane. This inner membrane appeared to coordinate the particles in a linear fashion throughout the lumen. Although limited in both cell types, viral particles were generally found more frequently and in greater abundance in hepatocytes than in HSC.

Interestingly, all HSC maintained their characteristic stellate morphology throughout the course of disease. Even those showing direct signs of infection, such as accumulation of viral particles in intracisternal spaces, appeared otherwise normal. While infected hepatocytes rapidly underwent apoptosis, HSC maintained prototypical morphology except for an apparently gradual loss of cytoplasmic lipid droplets that was complete by day 3 PI. Because of the loss of these characteristic vitamin A droplets, it was often difficult to discern HSC by routine H&E staining during the peak of liver pathology. However, ultrastructural examination revealed reduced numbers of HSC during the acute hepatitis phase compared to those in uninfected control mice. Despite being a target of infection themselves, abundant HSC of classical fine structure and diminished cytoplasmic lipid droplets were apparent again 6 day PI. These findings suggest their brisk proliferation in response to the damage in the previous days of infection, and the reappearance of their cytoplasmic lipid droplets after day 6 PI may indicate their return to a quiescent state after viral clearance from the liver.

Ultrastructural examination of the liver also revealed evidence of vascular injury and fibrin deposition. Polymerized fibrin was closely associated with the sinusoidal face of hepatocytes, and occluded perisinusoidal space in liver specimens from one mouse sampled on day 3 PI (Fig. 5). One mouse sampled 3 day PI and both mice sampled 4 day PI also showed extensive perivenular collagen deposits around central veins, possibly indicating a

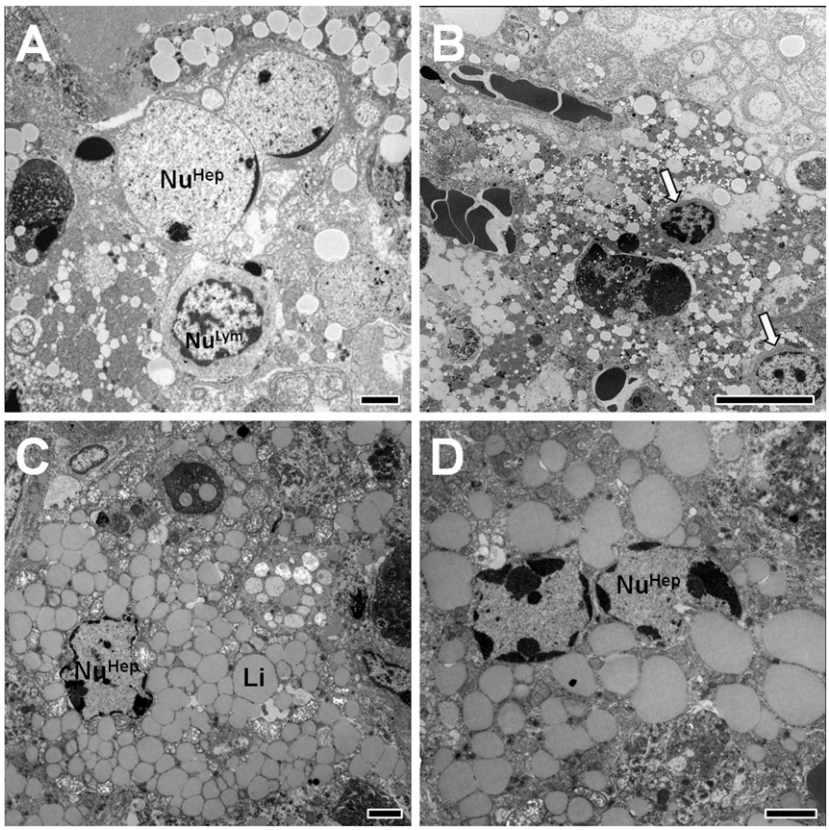

Fig. 3. Inflammatory mononuclear white blood cells morphologically consistent with lymphocytes were frequently associated with apoptotic hepatocytes; and lipid-type vacuolar degeneration of viable hepatocytes occurred 3 day PI. (A) Small, extravasated lymphocyte shows intimate association with the nucleus of an apoptotic hepatocyte (Nu^{Hep}) 3 day PI. (B) Lymphocytes (indicated by white arrows) adjacent to degenerate hepatocyte 3 day PI. Bars: (C and D) Representative images of rare hepatocytes that maintain viability 3 day PI. Heterochromatin clumps under the surface of the nuclear envelope, and the majority of the cytoplasm is filled with lipid (Li); which occludes organelles, cytoplasmic space, and other normal structures. Bars: A, C, and D = 2 μm; B = 10 μm.

fibrotic response to vascular injury. Collagen bundles were present in the perisinusoidal space and often spatially associated with HSCs. In conjunction with their loss of cytoplasmic lipid droplets, this demonstrated that HSCs entered an activated state and implicated their role in fibrogenesis during infection. Activated HSCs stimulate hepatocyte proliferation and secrete extracellular matrix components to promote liver regeneration. Disseminated extravasated erythrocytes were also a common finding in all animals during days 3 and 4 PI and indicate microhemorrhage. Along with inflammatory mononuclear and polymorphonuclear white blood cells, extravasated erythrocytes were found packed in the perisinusoidal space and distributed throughout the parenchyma, often adjacent to degenerate hepatocytes. These microhemorrhages were more severe and widespread in animals 4 day PI, where they were often seen to be associated with severely degenerate hepatocytes and fibrotic vessels.

Other prominent and common findings in the liver on days 3 and 4 PI included phagocytosis of apoptotic debris by infiltrating mononuclear blood cells and filamentous intranuclear inclusions of varying degrees of polymerization in hepatocytes (Fig. 6). These inclusion bodies represent production of a viral protein (Struthers and Swanepoel, 1982), and therefore indicate infection of the cell. Hepatocytes displaying these inclusion bodies often appeared otherwise structurally normal, perhaps indicating that they are in an early stage of infection during which they still maintain their viability.

A relatively robust sample of sinusoidal endothelial cells revealed essentially no ultrastructural changes in those examined. However, in samples acquired 3 and 4 days PI, the endothelium was either discontinuous or completely absent in areas of hepatic hemorrhage. Normal and continuous sinusoidal endothelia were observed in all liver specimens of both animals sampled 5 day PI and beyond, and contributed to the resumption of normal hepatic cord structure appearance. Viral particles and inclusion bodies were not observed in hepatic sinusoidal or venous endothelial cells at any time-point, suggesting that they may not be targets of direct infection.

Normal Kupffer's cells were observed 1 and 2 days PI. However, with the onset of acute liver disease 3 day PI, mononuclear white blood cells were frequently observed outside of the sinusoidal endothelial lumen in association with hepatocytes, even in areas where the endothelium was continuous. Many extravasated perisinusoidal white blood cells were morphologically consistent with Kupffer's cells and contained components of degraded cells in their lysosomal compartments. This suggests their possible influence contributing to hepatitis and phagocytosis of degenerate hepatocytes, which are both well-established roles of Kupffer's cells during viral infection (Kolios et al., 2006; Sitia et al., 2011). Kupffer's cells did not show evidence of direct infection at any time-point by EM, despite having shown RVF immunoreactivity 2 day PI and beyond in our prior study.

Later sampling days revealed a gradual but remarkably complete recovery of structure and clearance of visible virus and viral inclusion material. The livers of both animals sampled day 5 PI revealed recovery of defined sinusoidal structure that was lost during days 3 and 4 PI. However, degenerate hepatocytes and cellular debris still made up much of the parenchyma, and numerous extravasated inflammatory leukocytes were still present. The sinusoidal and venous endothelia were largely free of the indicators of damage observed earlier. By day 6 PI,

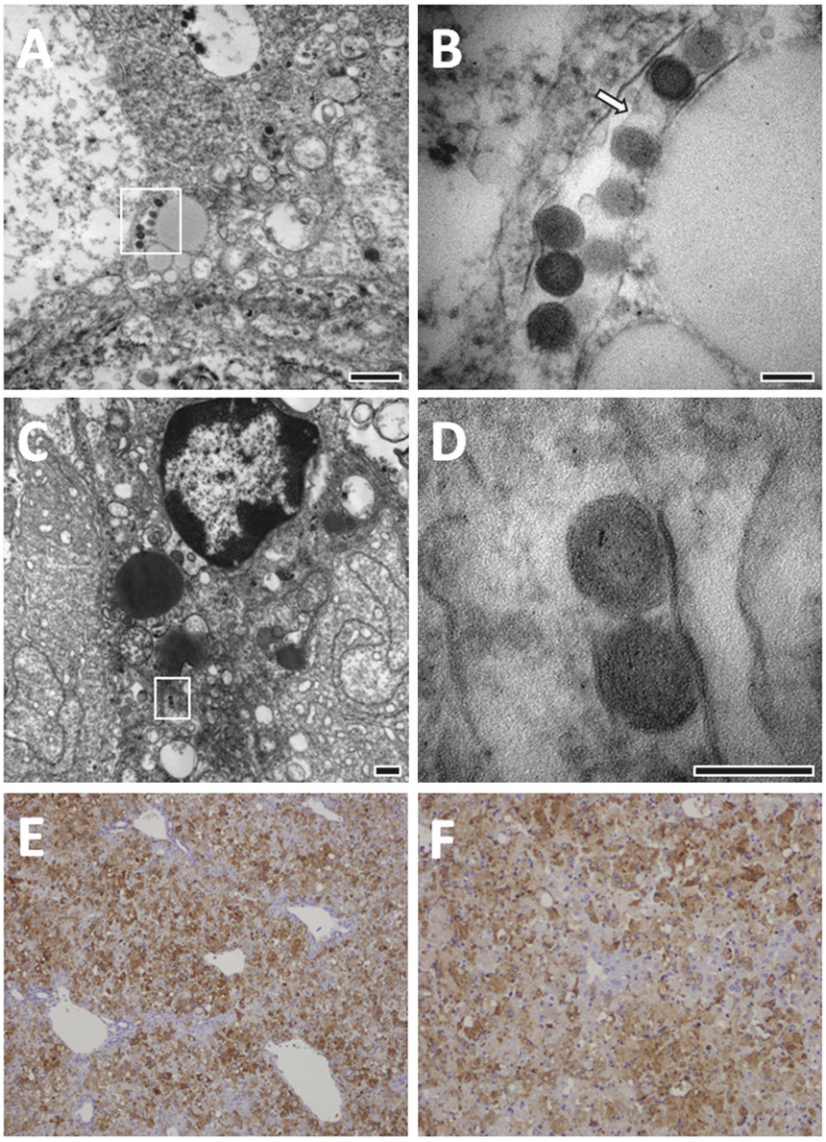

Fig. 4. Rare viral particles were observed by EM 3 day PI in hepatocytes and hepatic stellate cells, which is in contrast to IHC antigen detection. (A) Low-magnification image of viral particles accumulating in an intracytoplasmic membrane-bound body in a hepatocyte; presumably a vesicle originating from the Golgi complex. (B) High-magnification image shows details of particles observed in (A). 90–100 nm, electron-dense particles appear to be linearly coordinated. Interestingly, some particles appear to share a continuous membrane inside and separate from their enclosure within the cytoplasm (white arrow). (C) Hepatic stellate cell with contracted cytoplasmic lipid droplets contains two viral particles. (D) Details from (C) show particles coordinated along continuous membrane. (E and F) Immunohistochemistry demonstrates the amounts of RVFV antigen in the livers. Bars: A and C=500 nm; B and D=100 nm.

hepatocytes were beginning to regain normal ultrastructure including intercellular junctions, although most maintained numerous fat vacuoles and pale cytoplasm. The eighth and final day of sampling revealed an essentially complete reversion to the undiseased state, with some apparently aberrant lipid droplets lingering in hepatocytes (Fig. 7).

Ultrastructural changes in the central nervous system (CNS)

The most significant observation in the CNS was direct evidence of infection of neurons and neuroglial cells in the spinal cord and brainstem. RVFV replication and cytoplasmic viral particle accumulation were first observed in cells morphologically consistent with microglia and astrocytes of the spinal cord on day 5 PI. On day 6 PI, mature and budding viral particles accumulated in microglial cells, astrocytes, and neurons of the spinal cord and brain stem (Fig. 8). Similarly, a significant amount of viral antigen was detected in the brainstem by immunohistochemsitry (spinal cord not sampled; Fig. 8). In infected neurons, viral particles accumulated exclusively in the soma; specifically, in the cisternae of the Golgi apparatus, and the lumen of the ER. Particles were not observed in the organelle-sparse axonal or dendritic projections at any time-point. Similarly, budding and fully formed RVFV particles were primarily observed in the Golgi and ER cisternae of neuroglial cells. Viral budding appeared to be spatially related to the nucleus, with a greater proportion of particles appearing in the ER directly adjacent to the nuclear envelope than close to the plasma membrane.

The concentration of viral particles in CNS tissues appeared to peak at day 6 PI, at which point virtually all astrocytes and neurons sampled from the spinal cord contained numerous enveloped particles in all planes of section. Infection of the brainstem, while present and progressive, appeared to be more moderate in severity. Most visible viral particles were bound within the Golgi cisternae and ER, which were generally swollen and accompanied by degeneration of other membrane-bound

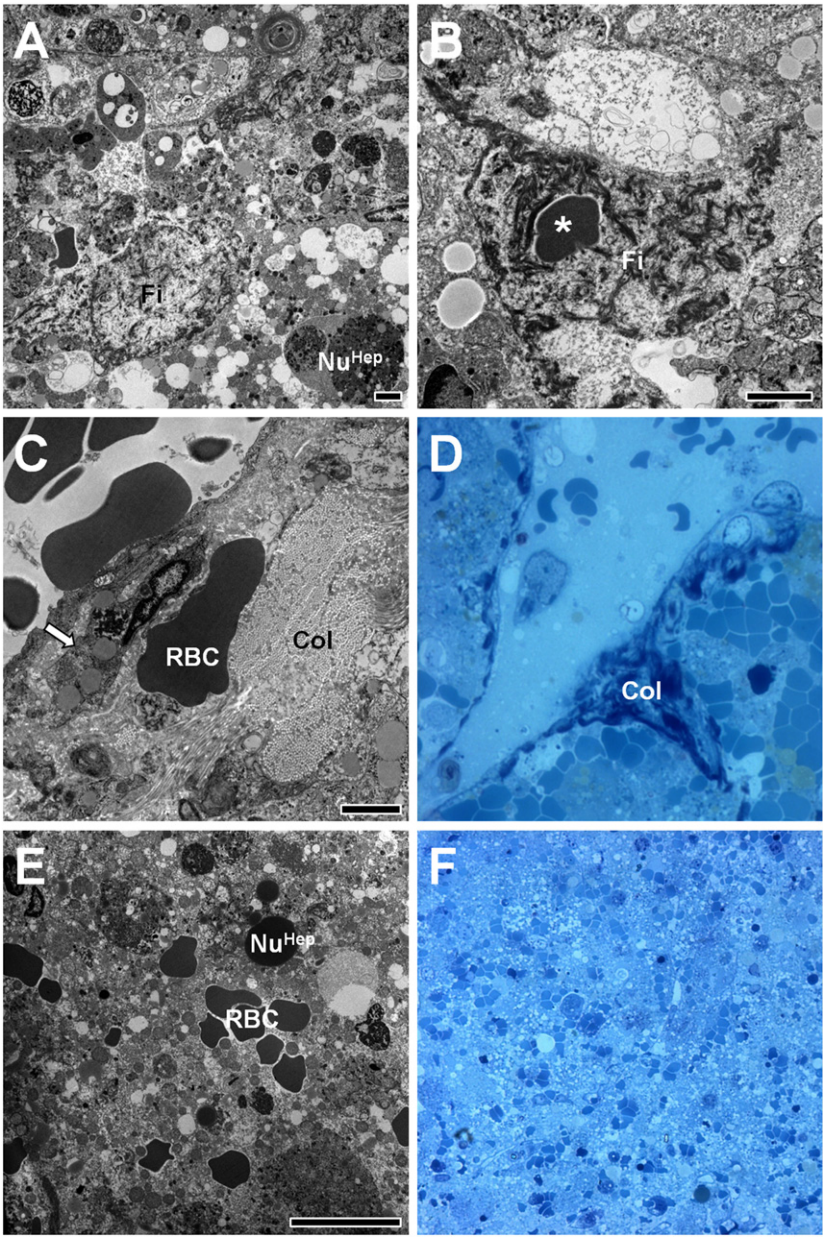

Fig. 5. Fibrin polymerization, collagen deposition, and hemorrhage appeared in the liver 3 and 4 days PI. (A) Polymerized fibrin (Fi) appears as electron-dense, brush-like structures throughout the sinusoidal blood, and especially on the villous face of hepatocytes. A degenerate hepatocyte with necrotic nucleus (Nu^{Hep}) is visible in this field of a tissue section acquired 3 day PI. (B) Fibrin encloses a red blood cell (asterisk) in circulation 3 day PI. (C) Large tracts of collagen (Col) are cut both in cross-section and longitudinally, rendering distinct appearances when viewed by EM. A red blood cell (RBC) outside of circulation appears between collagen deposits and an activated matrix-producing, or hepatic stellate, cell (white arrow) 3 day PI. (D) Light micrograph of a section of central vein from an animal sampled 4 day PI shows large, dark-staining deposits of collagen (Col) along the basal aspect of the sinusoidal endothelium. Inflammatory cells and debris are present in the vessel's lumen. Magnification = 1000 ×. (E) With much of the normal hepatic ultrastructure obliterated, red blood cells (RBC) are frequently observed outside of remaining vessels. (F) Representative light micrograph shows the extent of liver damage and accompanying hemorrhage 4 day PI. Red blood cells are observed almost exclusively outside of discernible sinusoids throughout the parenchyma. Magnification = 400 ×. Bars: A–C = 2μm; E = 10μm.

cytoplasmic organelles. However, host cell nuclei appeared normal and plasma membrane integrity was always maintained. The spinal cord and brain stem of animals sampled at day 8 PI showed a similar degree of cytopathology and particle accumulation as those on day 6 PI.

Interestingly, analyses of multiple cerebrum samples from each animal in the study yielded no discernible virus at any time-point. Findings outside of the brainstem and spinal cord were limited to perivascular edema in all animals 3 day PI and later, as well as nonspecific osmotic dysfunction in the neuropil resulting in swelling of mitochondria and perinuclear space in neurons and neuroglia as compared to control tissues from uninfected animals. This effect was most pronounced later in infection, and was also apparent in the brainstem and spinal cord where viral particles were abundant.

Ultrastructural changes in the secondary lymphoid organs

The primary ultrastructural lesion in the spleen and lymph nodes was overwhelming lymphocytolysis via apoptosis. Viral particles were not observed directly in any cell type in these organs despite being detected by IHC in the previous study. At 3 and 4 days PI, nearly all lymphocytes sampled appeared degenerate, with the majority displaying changes indicative of

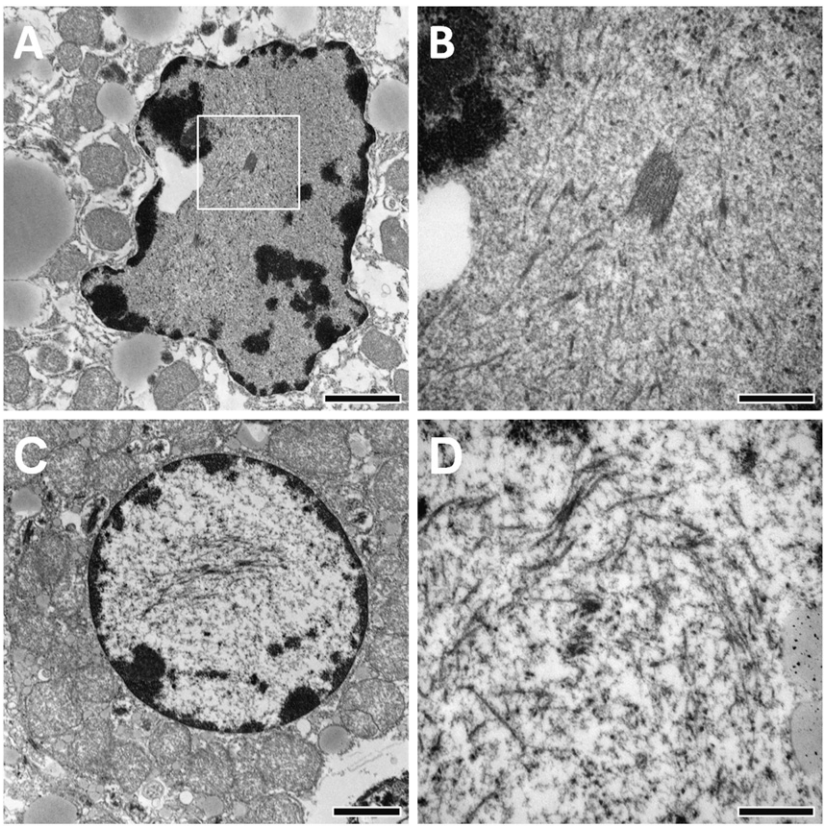

Fig. 6. Intranuclear inclusions of varying degrees of polymerization were found in viable hepatocytes 3 and 4 days PI. (A) The nucleus of a hepatocyte sampled 3 day PI shows many electron-dense, monomeric filaments; aligned approximately in parallel. Fibrils are only found in association with euchromatin. (B) High-magnification image of a polymerized bundle of filaments visible in (A). These highly ordered, polymerized arrays were observed much less frequently than unpolymerized filaments. (C) Hepatocyte from an animal sampled 4 day PI shows a similar inclusion, with loosely coordinated fibers spanning most of the nucleus. (D) Higher-magnification image of poorly coordinated, unpolymerized intranuclear inclusions. Bars: A and C=2 μm; B and D=500 nm.

apoptosis (Fig. 9). Apoptotic plasma cells were also frequently observed in the spleen and lymph nodes days 6–8 PI, although it is unclear if this cell death was a physiological consequence of reduced demand for antigen-specific antibodies (Ursini-Siegel et al., 2002) or induced by viral infection. Additionally, numerous tingible body macrophages (TBM) were apparent in all lymph node specimens from all mice examined on days 3–6 PI. The frequency and proximity of these TBM suggests increased germinal center proliferation and phagocytosis of apoptotic lymphocytes, particularly in light of their appearance after day 3 PI. Also, the proportion of neutrophils in the spleen and lymph nodes increased greatly from days 3 to 6 PI, reflecting the systemic nature of granulocytic inflammation. Finally, ultrastructural changes were also observed in viable plasma cells and fibroblastic reticular cells (FRC). These cells showed swollen organelles, and vesicular degeneration 3 and 4 days PI.

Ultrastructural changes in other tissues

Ultrastructural lesions outside of the liver, CNS, and lymphoid tissues were generally sporadic and minimal in the tissues sampled. Viral particles were not directly observed during analysis of kidney, heart, gonad, eye, or lung tissues. The most significant observations were of RVFV-specific microfibrillar intranuclear inclusions in endothelial cells of the heart and kidneys (Fig. 10). In particular, the specialized glomerular endothelium showed prominent and highly polymerized inclusion bodies. Coincident with the peak of liver cytopathology and inflammation, endothelial intranuclear inclusion bodies were most abundant on days 3 and 4 PI; and were also observed in numerous hepatocytes on those days. These inclusion bodies were preferentially associated with host euchromatin, and were found as either discrete, highly ordered bundles; or numerous, disseminated, and unpolymerized fibers oriented in roughly the same direction.

Discussion

Our findings generally complement and expand upon the immunohistochemistry and histopathology observations presented previously (Smith et al., 2010), with a few notable exceptions. In particular, the rarity of viral particles in liver tissues sampled and their abundance in the basal structures of the CNS represent a considerable divergence from expectations set by IHC and histopathology in those tissues. For example, by 3 day PI, nearly 80% of hepatocytes stained via IHC for RVFV antigen; however, observation of viral particles was exceedingly rare in any cell type of the liver. Synthesis of viral components (as evidenced both by immunoreactivity and inclusion body formation) in the absence of mature particle production indicates that many hepatocytes may undergo abortive infection, or undergo apoptosis before release of mature RVF virions. This is in stark contrast to infected cells in the CNS, which accumulated classical RVFV particles to abundance during infection despite failing to show significant degenerative changes by EM. This is also in contrast to other viruses that cause hemorrhagic fever, such as Marburgvirus and Ebolavirus, in which viral particles are easily discernible throughout the course of infection by EM in target

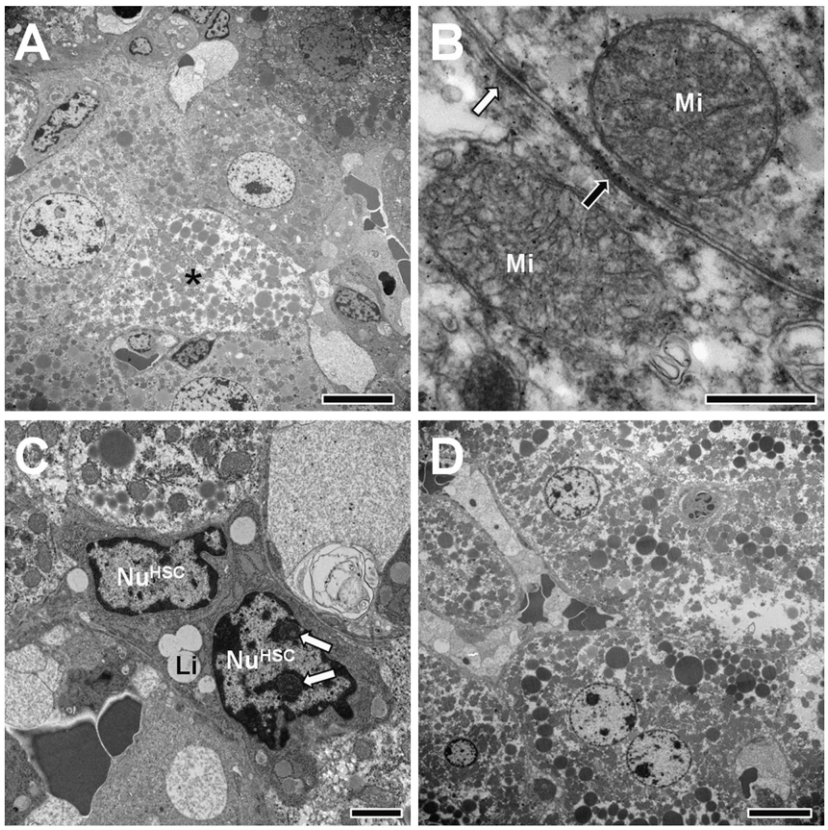

Fig. 7. Liver began to regain normal ultrastructure 6 day PI, with nearly complete recovery by 8 day PI. (A) Low-magnification image from a liver sample obtained 6 days PI shows resumption of higher sinusoidal structure. One hepatocyte in this field still maintains atypically pale cytoplasm, as well as dense cytoplasmic lipid droplets. (B) High-magnification image of lateral junctional complexes between two hepatocytes 6 days PI. Gap junction (black arrow) and tight junction (white arrow) resemble those observed in control animals and prior to acute disease. Mitochondrial (Mi) ultrastructure also appears normal. (C) Representative image of sub-sinusoidal endothelial space shows two cells morphologically consistent with hepatic stellate cells during post-activation recovery of cytoplasmic lipid droplets (Li). Lipid droplets are smaller and more dispersed than those observed prior to 3 day PI. One cell in this field has two prominent nucleoli (white arrows), also suggesting a state of activation. Stellate cells were abundant during the liver repair and recovery phase of RVFV infection. (D) Representative low-magnification EM of liver sampled 8 day PI shows normal ultrastructure with some lingering aberrant lipid deposition and nuclei rich in euchromatin. Bars: A and D=10 μm; B=500 nm; C=2 μm.

tissues; and cytopathology and cell death are always associated with infection (Bradfute et al., 2007; Hensley et al., 2011). Additionally, cells labeled by IHC in models of Marburg and Ebola hemorrhagic fevers generally agree well with ultrastructural localization of viral particles and budding events (Geisbert et al., 1992; Hensley et al., 2011). However, the rare ultrastructural observation of mature RVF viral particles in tissues expected to be a major site of viral replication (via IHC and cytopathology) in the current model is shared with Lassa virus, which is also classified as a virus causing hemorrhagic fever (Reed, unpublished observations).

The comparatively infrequent observation of viral particles and extremely early and sudden onset of such catastrophic tissue damage may suggest a primarily host immune-mediated mechanism, rather than uncontrolled mature viral particle proliferation, for liver disease and dysfunction during RVFV infection. Early infiltration by both mono- and polymorphonuclear white blood cells indicates a robust leukochemotactic response in the liver, and cell junction dissolution was previously shown to be effected by cytotoxic inflammatory cytokines (Capaldo and Nusrat, 2009; De Maio et al., 2000; Yamamoto et al., 2004). Complete blood count (CBC) analysis from the previous study showed an increase from 20% circulating neutrophils in peripheral blood drawn pre-exposure to over 70% 3 day PI. Neutrophils have an important role associated with liver cell disruption and death during aseptic hepatitis (Jaeschke, 2002), and neutrophilic extravasation was prominent in the current study both by EM and histology. Cytokine quantification data from the previous study also show significant increases in pro-inflammatory cytokines throughout infection, with a peak 3–4 days PI that is coincident with greatest liver pathology (Smith, unpublished observations). These factors include TNF-α, a known mediator of neutrophilic hepatitis (Jaeschke, 2006), as well as other inflammatory conditions. Additionally, a recent study in mice showed a strong correlation between cytokine induction and RVFV pathogenicity (Gray, 2012). Infection with the virulent, wild-type strain of RVFV induced a much more robust immune response as determined by quantification of cytokines in sera and liver tissues than a nonlethal, attenuated strain. In particular, individual mice with higher levels of inflammatory and chemotactic cytokines, such as IL-1α, IL-6, IFN-γ, and G-CSF, exhibited a more severe liver disease than their counterparts with lower cytokine levels (Gray, 2012). Finally, it has been shown that certain antiviral cytokines contributed to the morbidity and mortality of mice experimentally infected with Punta Toro virus, a phlebovirus related to RVF (Gowen et al., 2006).

One limitation of EM by design is its relatively small sampling of tissue. In order to maximize our confidence in the rarity of viral particles observed in the liver, we increased the scope of our EM investigation to include over 90 individual samples of liver tissue from 82 mice sampled days 1–8 PI (Smith, unpublished). By utilizing these additional samples, we were able to confirm that the extremely rare appearance of RVF viral particles in the liver was not an anomaly. The positive identification of viral particles in hepatocytes and HSC on very rare occasions confirms the

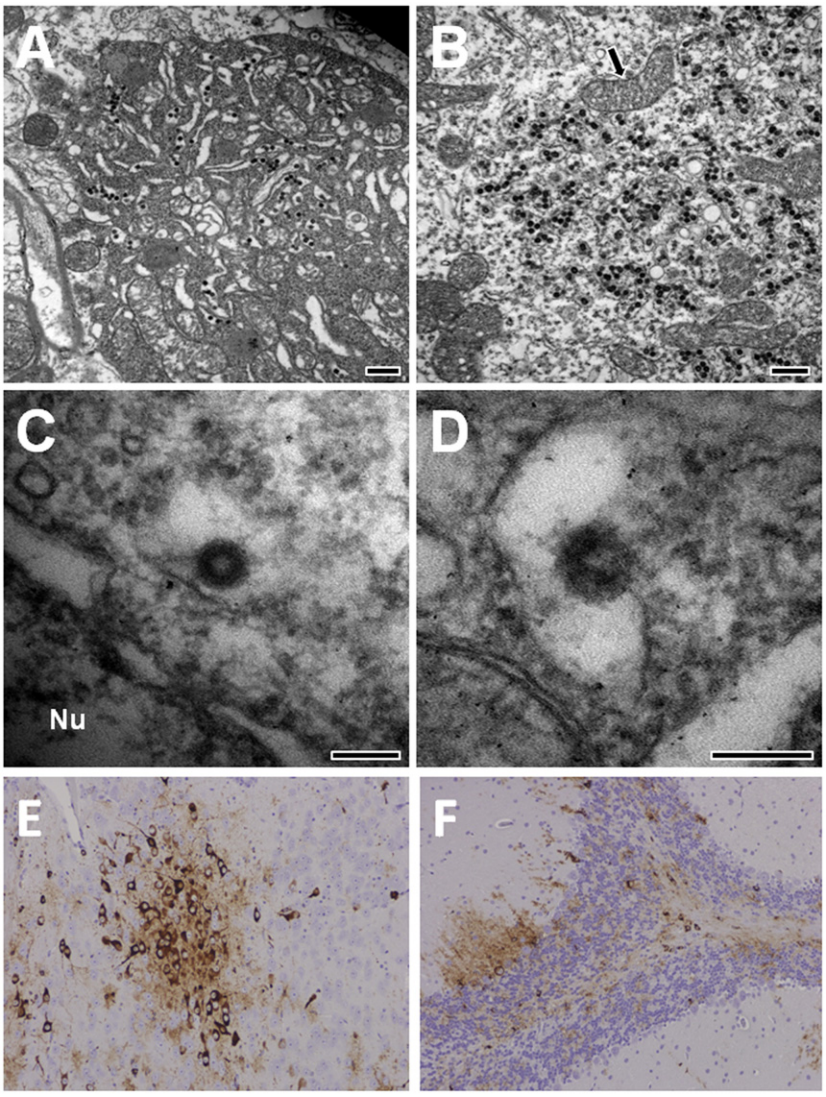

Fig. 8. Despite absence of neurocytopathology, abundant viral particles were observed budding and accumulating in multiple cell types of the central nervous system 6 days PI and later. (A) Abundant electron-dense, 90–100 nm spherical particles accumulate in membrane-bound bodies in the cytoplasm of a neuroglial cell. A bean-shaped nucleus (not shown in this image) and cytoplasmic lysosomes suggest that this cell may be an activated microglial cell. (B) Massive quantities of viral particles were found in a neuron of the spinal cord 6 day PI. Despite the number of particles present, organelles such as mitochondria (arrow) appeared normal. (C) High-magnification image of a discrete, fully formed viral particle. The particle appears to have an electron-lucent center in this preparation. (D) High-magnification image of a particle apparently in the process of budding into a smooth-walled vesicular lumen. The particle's envelope membrane appears to be continuous with the host cell's vesicle membrane. (E and F) RVFV antigen is abundant in the brainstem by immunohistochemistry on day 8 PI. Bars: A and B=500 nm; C and D=100 nm.

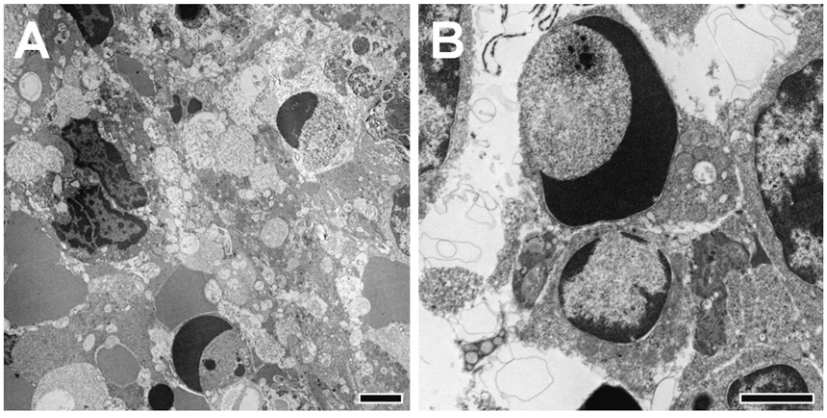

Fig. 9. Most splenic lymphocytes appear to undergo apoptosis around 4 day PI. (A) Two small lymphocytes show the classical heterochromatin crescent nuclear configuration associated with apoptosis 4 day PI. The tissue contains necrotic debris and red blood cells. (B) Two small lymphocytes undergo apoptosis 5 day PI. Note the increased intercellular space from day 4. All bars=2 μm.

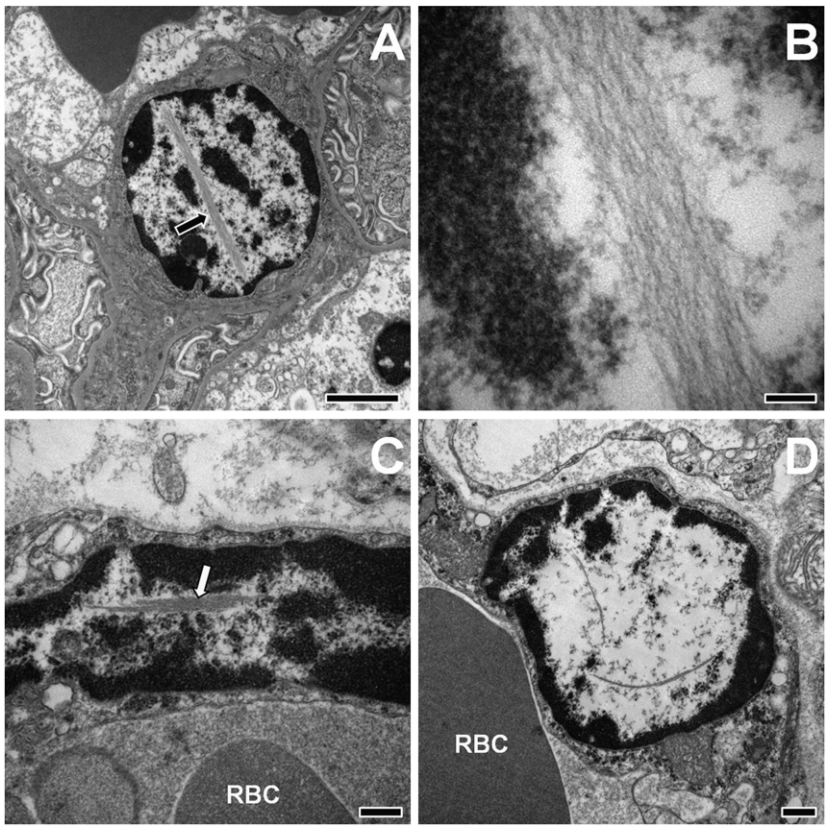

Fig. 10. Microfibrillar intranuclear viral inclusion bodies are prominent in endothelial cells and show differing degrees of polymerization 3 and 4 days PI. (A) A large, straight, highly organized inclusion body in a glomerular endothelial cell, 4 day PI. The inclusion is composed of filaments 5–10 nm in diameter running in parallel longitudinally, and appears to be preferentially associated with euchromatin. (B) High-magnification image shows detail of individual fibrils. (C) A short, brushlike inclusion in a cardiac endothelial cell 4 day PI. Heterochromatin is clumped under the surface of the nuclear envelope, leaving a euchromatic nuclear center in which the inclusion is resolved. (D) Cardiac endothelial cell shows long, narrow, rope-like inclusions. High-magnification examination of these structures reveals them to be composed of the same fibrillar components as in other tissues. Bars: A=2 μm; B and C=100 nm; D=500 nm.

sensitivity of the EM as a means of RVF viral particle detection. Another possible explanation for the rarity of direct observation of RVFV particles in the liver is that the time-points selected for tissue sampling failed to capture the peak of mature viral production in the liver. Published EM observations of RVFV infection in vitro and in mice attest to its rapid growth in both models; with discernible viral particles appearing 12 h PI in hepatocytic cell culture (Anderson and Smith, 1987), and 4 h PI or earlier in hepatocytes of a mouse model utilizing a high infectious dose (McGavran and Easterday, 1963). However, it must be reiterated that in the current model, peak immunohistochemical staining in the liver was achieved 3 day PI, and samples analyzed 1 day PI were absolutely devoid of both viral particles and indicators of cytopathology via EM. Therefore, it seems unlikely that viral proliferation could have occurred by 1 day PI without resulting in observation of cytopathology or viral particles.

When particles were observed in the liver, they often appeared to be coordinated in a linear fashion and bound by a separate membrane inside the Golgi lumen. This phenomenon has been previously described via EM of RVFV particles both inside hepatocytes and recovered from rodent sera (Ellis, 1977). It is unclear if this represents an aberrant budding event, such as packing of multiple viral nucelocapsids into a shared envelope. Interestingly, this structure was only noted in particles budding in hepatocytes. A similar phenomenon has been observed for filoviral particles budding in cell culture (Beniac et al., 2012), and has been characterized for baculoviruses (Washburn et al., 1999).

The earliest pathologic change observed in any organ system was the appearance and expansion of intercellular space along the lateral aspect of many hepatocytes in the liver, a lesion suggestive of dissolution of lateral junction complexes. This change occurred by 2 day PI, a day before any other ultrastructural lesions were apparent in any organ. It has been established that inflammatory cytokine transduction results in tight junction reorganization and reduction in cultured hepatocytes (Yamamoto et al., 2004) and rapid hepatocytic gap junction disappearance in rats (De Maio et al., 2000). Hepatocytic individualization has previously been reported as an early consequence of RVF infection (Gray, 2012; McGavran and Easterday, 1963); but EM examination provided direct observations of dissolution of interhepatocytic junctions as a direct predecessor to this event. Additionally, junction dissolution may be due to cellular swelling; a nonspecific pathogenic event associated with osmotic dysfunction that eventually leads to intercellular space expansion and individualization of cells (Cheville, 2009). Clearly defined hepatocytic junctional complexes did not reappear again until 6 day PI.

Infiltration of the liver by cells morphologically consistent with monocytes and macrophages was common 3 and 4 days PI. Mononuclear cells often had multiple cytoplasmic lysosomes containing cellular remains. Monocytic lineage cells were previously observed to be RVF antigen-positive by IHC (Smith et al., 2010) and susceptible to infection in culture (Lewis et al., 1987), and may be critical to the process of viral spread to other organ systems; such as the endothelium and CNS. The significant delay between the onset of hepatitis (3 day PI) and appearance of viral

particles in the CNS (5 day PI) also supports the suggestion of viral dissemination via mononuclear blood cells after primary infection and modest amplification in the liver.

EM observations also revealed viral inclusion bodies in endothelial cells of other organ systems; implicating direct infection of these cells as a possible means of vascular injury. Similar to the majority of hepatocytes sampled, viral inclusion bodies in endothelial cells were not accompanied by mature particles. Additionally, the finding of extravascular erythrocytes in the liver parenchyma represents the first observation of RVFV-associated hemorrhagic syndrome in the present BALB/c mouse model. Hepatic microhemorrhages were disseminated throughout the acute hepatitis phase of disease in both animals sampled 3 and especially 4 day PI. Fibrin deposition on the sinusoidal endothelium in one animal 3 day PI also indicated vascular injury, and polymerization in sinusoidal blood suggests onset of coagulopathy that correlates to hemorrhagic manifestations similar to other viral hemorrhagic fevers (Geisbert et al., 2003; Srichaikul et al., 1977; Steele et al., 2009) and severe human cases of RVF (Abdel-Wahab et al., 1978). Despite no evidence of hemorrhagic disease histologically in our previous study, the transience of this manifestation in the current ultrastructural study suggests that an adjustment to infectious dose and/or sampling time may be required to produce an optimal model of hemorrhagic disease. Additional studies should provide further insight about the use of the mouse model to portray hemorrhagic disease manifestations.

The ultrastructural picture of infection and pathogenesis in the CNS appears to be the opposite of the liver. For example, findings included underwhelming neurocytopathology, late appearance of viral particles, and progressive and massive proliferation of RVFV particles in susceptible neurons and neuroglia. Likewise, in all sections examined, there was an absence of circulating inflammatory cell invasion into the neuropil. Despite the appearance of cerebral edema after day 3 PI, the specialized cerebral endothelium responsible for maintaining the blood–brain barrier appeared to be intact without exception, and the tight junctions between these endothelial cells were intact throughout the study. These observations suggest that late neurological manifestations are related to direct infection of CNS neurons and their supporting cells by RVF. The immunologically privileged status of the CNS may contribute to this uncontrolled viral expansion and help explain the scarcity of cytopathic effect and cell death in these tissues.

This study offers further insight into the means and temporality of RVFV neuroinvasion after peripheral exposure. Essentially, there was a gradual infection of spinal cord followed by basal brain tissues; while viral particles were not observed in higher cerebral structures by EM, likely due to a failure to reach a uniform concentration sufficient for detection. This was interesting in light of plaque assay results from a separate cohort of mice that showed similar concentrations of infectious virus in the liver 4 day PI and brain 6 day PI. Despite finding rare viral particles in liver samples 4 day PI, the lack of any mature viral particles in the cerebrum at any time-point is likely an effect of the heterogeneity of viral concentration throughout the brain. RVFV particles appeared to accumulate in the basal structures of the CNS, and inclusion of cells from these areas in the relatively large sample analyzed in the plaque assay could explain the overall tissue titer equal to that of the liver. The smaller sample size and more precise acquisition of samples for EM yielded observation of abundant viral particles in the spinal cord and brainstem, but not in the cerebrum.

Viral particles were first observed 5 day PI in the thoracic spinal cord, where they proliferated to reach massive quantities in the days following. Cells of the brainstem were infected 6 day PI, but significantly fewer virions were observed per cell and a greater proportion of cells appeared uninfected than in the spinal cord at the same time-point. Over days 7 and 8 PI, brainstem infection appeared to increase in magnitude as judged by the proportion of cells infected and the number of viral particles per cell. No virus was observed at any time-point in cerebral samples. In light of this cephalic progression of visible particles, we posit that RVFV may enter and infect the brain by reproduction in large neurons of the immunologically accessible spinal cord, which provides direct cell contact with the neurons and supporting cells of the brainstem. Productive infection of the brainstem then allows viral contact with multiple structures of the cerebrum. RVF antigen immunoreactivity was previously demonstrated on this level of the brain in mice sampled on day 8 PI (Smith et al., 2010) from this study. Future attempts to elucidate the mechanisms of CNS invasion by RVF should include analyses of peripheral nerves, as neurons of the PNS that are proximal to the site of infection may be subject to even earlier infection; and of the olfactory tract, which provides another route of access to the brain.

In addition to further characterizing RVF pathogenesis of the liver and CNS, EM identified abundant intranuclear filamentous inclusion bodies in hepatocytes and endothelial cells of the heart and glomeruli. These inclusion bodies have been previously noted by light microscopy in cell culture and tissues from livestock infected with RVFV as intranuclear eosinophilic masses (Abdel-Wahab et al., 1978; Kamal, 2009), characterized by EM of infected cell culture (Ellis et al., 1988; Swanepoel and Blackburn, 1977; Yadani et al., 1999), and in hepatocytes from infected mice (Ellis, 1977). To the best of our knowledge, the current observations represent the first EM studies of these structures in endothelial cells. These microfibrillar bundles have previously been shown to be aggregates of filamentous viral proteins with a diameter of 5–10 nm, and are diagnostic of RVFV infection and viral protein production (Struthers and Swanepoel, 1982; Yadani et al., 1999). Therefore, despite the absence of direct visualization of viral particles in endothelial cells in the current study, the abundance of viral inclusion bodies suggests their contemporaneous infection with the liver on days 3 and 4 PI. However, the lack of viral budding associated with the endothelium may also indicate an abortive or otherwise nonproductive infection.

Despite the magnitude of cell death, and in accordance with previous findings by immunohistochemistry (Smith et al., 2010), lymphocytes were never observed to be infected with RVFV by EM. Therefore, it seems likely that apoptotic lymphocytolysis during RVFV infection is a "bystander" effect as previously reported for other viral hemorrhagic fevers (Bradfute et al., 2010; Geisbert et al., 2000). While no other cell types in the lymphoid tissues were observed to contain viral particles by EM, dendritic cells and FRC have previously been shown to be RVFV-antigen positive by IHC. The relative infrequence of these cell types observed in the small samples prepared for EM may explain the lack of direct observation of virus in the spleen and lymph nodes, as uninfected small lymphocytes made up the vast majority of the volume in these tissues.

In conclusion, this study provides further insight into the pathogenesis of RVFV in the mouse model that has important implications for understanding RVF disease. Immune-mediated mechanisms most likely play an important role in causing acute-onset hepatitis, the dominant pathological feature of RVFV. Further insight into these mechanisms may provide potential targets for therapeutic intervention. Additionally, our study provides insight for the potential route of RVFV neuroinvasion and suggests that the mouse model may serve as a good model for hemorrhagic RVF disease.

Materials and methods

Study design

Samples for transmission electron microscopy (EM) analysis were obtained from the study previously described by Smith et al.

(2010). Briefly, female BALB/c mice were obtained from the National Cancer Institute, Frederick Cancer Research and Development Center (Frederick, MD), and were used when 6–8 weeks old. Mice were housed in microisolator cages and were provided water and chow ad libitum. For this study, mice were challenged subcutaneously with a target dose of 1000 plaque forming units of RVFV in a total volume of 100 μL. Two mice were euthanized on each of days 0–6 and 8 PI, and their tissues were collected at necropsy for comparative EM analysis.

Research at USAMRIID was performed in compliance with the Animal Welfare Act and other federal statutes and regulations relating to animals and experiments involving animals, and adheres to principles stated in the guide for the Care and Use of Laboratory Animals, National Research Council, 1996. USAMRIID is fully accredited by the Association for the Assessment and Accreditation of Laboratory Animal Care International.

Sample accession

Immediately following euthanasia, mice were necropsied and sections of liver, heart, lung, spleen, axillary lymph node, brain, spinal cord, and kidney were excised and immediately immersed in a 0.1 M cacodylate-buffered solution of 3% paraformaldehyde and 1.5% glutaraldehyde fixative. While still submerged in fixative, organs were trimmed into approximately 1 mm^3 pieces for primary fixation and routine EM processing.

EM sample processing and analysis

Samples were prepared for conventional transmission EM essentially as previously described (Perkins and McCaffery, 2007). Briefly, tissues were fixed overnight at 4 °C in 0.1 M cacodylate-buffered 3% paraformaldehyde and 1.5% glutaraldehyde, and then removed from biosafety level (BSL)-3 biocontainment in Pallade's veronal-buffered 1% osmium tetroxide. After 1 h osmication, tissues were stained en bloc overnight with Kellenberger's veronal-buffered 0.5% uranyl acetate. Samples were dehydrated with a graded series of ethanol and propylene oxide washes, and then infiltrated overnight with EMbed-812 resin (EM Sciences, Hatfield, PA) before embedment in BEEM capsules and polymerization at 60 °C for 48 h. Semi-thin (500 nm) and ultra-thin (50 nm) sections were cut with a Leica UTC ultramicrotome (Leica Microsystems Inc., Buffalo Grove, IL). Semi-thin sections were adhered to borosilicate slides, stained with basic 1% toluidine blue dye for 5 min, and then examined with a Nikon Eclipse 50i light microscope (Nikon Instruments, Melville, NY). At least two specimens of each tissue from each animal were then examined via thin-section with a JEOL JEM-1011 TEM (JEOL USA, Waterford, VA) without further staining. Images were acquired with a DVC CCD (DVC, Austin, TX) utilizing AMT v6 digital imaging software (AMT, Woburn, MA). Post-processing of images, including general adjustments to brightness and sharpness, was performed using Adobe Photoshop CS4.

Acknowledgments

We thank John Braun and Andrew Chrovian for their expert technical assistance with electron microscopic processing and sectioning. This work was supported by the Defense Threat Reduction Agency. The views of the authors do not necessarily reflect the position of the Department of Defense or the Department of the Army.

References

Abdel-Wahab, K.S., El Baz, L.M., El-Tayeb, E.M., Omar, H., Ossman, M.A., Yasin, W., 1978. Rift Valley fever virus infections in Egypt: pathological and virological findings in man. Trans. R. Soc. Trop. Med. Hyg. 72, 392–396.

Abu-Elyazeed, R., el-Sharkawy, S., Olson, J., Botros, B., Soliman, A., Salib, A., Cummings, C., Arthur, R., 1996. Prevalence of anti-Rift-Valley-fever IgM antibody in abattoir workers in the Nile delta during the 1993 outbreak in Egypt. Bull. World Health Organ. 74, 155–158.

Anderson Jr., G.W., Smith, J.F., 1987. Immunoelectron microscopy of Rift Valley fever viral morphogenesis in primary rat hepatocytes. Virology 161, 91–100.

Beniac, D.R., Melito, P.L., Devarennes, S.L., Hiebert, S.L., Rabb, M.J., Lamboo, L.L., Jones, S.M., Booth, T.F., 2012. The organisation of Ebola virus reveals a capacity for extensive, modular polyploidy. PLoS One 7, e29608.

Bird, B.H., Ksiazek, T.G., Nichol, S.T., Maclachlan, N.J., 2009. Rift Valley fever virus. J. Am. Vet. Med. Assoc. 234, 883–893.

Bradfute, S.B., Braun, D.R., Shamblin, J.D., Geisbert, J.B., Paragas, J., Garrison, A., Hensley, L.E., Geisbert, T.W., 2007. Lymphocyte death in a mouse model of Ebola virus infection. J. Infect. Dis. 196 (Suppl. 2), S296–S304.

Bradfute, S.B., Swanson, P.E., Smith, M.A., Watanabe, E., McDunn, J.E., Hotchkiss, R.S., Bavari, S., 2010. Mechanisms and consequences of ebolavirus-induced lymphocyte apoptosis. J. Immunol. 184, 327–335.

Capaldo, C.T., Nusrat, A., 2009. Cytokine regulation of tight junctions. Biochim. Biophys. Acta 1788, 864–871.

Cheville, N.F., 2009. Ultrastructural Pathology: The Comparative Cellular Basis of Disease, 2nd ed. Wiley-Blackwell, Amesterdam, IA.

Daubney, R., Hudson, J., Garnham, P., 1931. Enzootic hepatitis or Rift Valley fever: an undescribed virus disease of sheep, cattle and man from East Africa. J. Path. Bacteriol. 34, 545–579.

De Maio, A., Gingalewski, C., Theodorakis, N.G., Clemens, M.G., 2000. Interruption of hepatic gap junctional communication in the rat during inflammation induced by bacterial lipopolysaccharide. Shock 14, 53–59.

Ellis, D.S., et al., 1977. Rift Valley fever virus: some ultrastructural observations on material from the outbreak in Egypt 1977. J. Gen. Virol. 42, 8.

Ellis, D.S., Shirodaria, P.V., Fleming, E., Simpson, D.I., 1988. Morphology and development of Rift Valley fever virus in Vero cell cultures. J. Med. Virol. 24, 161–174.

Geisbert, T.W., Hensley, L.E., Gibb, T.R., Steele, K.E., Jaax, N.K., Jahrling, P.B., 2000. Apoptosis induced in vitro and in vivo during infection by Ebola and Marburg viruses. Lab. Invest. 80, 171–186.

Geisbert, T.W., Hensley, L.E., Larsen, T., Young, H.A., Reed, D.S., Geisbert, J.B., Scott, D.P., Kagan, E., Jahrling, P.B., Davis, K.J., 2003. Pathogenesis of Ebola hemorrhagic fever in cynomolgus macaques: evidence that dendritic cells are early and sustained targets of infection. Am. J. Pathol. 163, 2347–2370.

Geisbert, T.W., Jahrling, P.B., Hanes, M.A., Zack, P.M., 1992. Association of Ebola-related Reston virus particles and antigen with tissue lesions of monkeys imported to the United States. J. Comp. Pathol. 106, 137–152.

Gowen, B.B., Hoopes, J.D., Wong, M.H., Jung, K.H., Isakson, K.C., Alexopoulou, L., Flavell, R.A., Sidwell, R.W., 2006. TLR3 deletion limits mortality and disease severity due to Phlebovirus infection. J. Immunol. 177, 6301–6307.

Gray, K.K., et al., 2012. Chemotactic and inflammatory responses in the liver and brain are associated with pathogenesis of Rift Valley fever virus infection in the mouse. PLoS Neg. Trop. Dis., 6.

Hensley, L.E., Alves, D.A., Geisbert, J.B., Fritz, E.A., Reed, C., Larsen, T., Geisbert, T.W., 2011. Pathogenesis of Marburg hemorrhagic fever in cynomolgus macaques. J. Infect. Dis. 204 (Suppl. 3), S1021–S1031.

Jaeschke, H., 2002. Neutrophil-mediated tissue injury in alcoholic hepatitis. Alcohol 27, 23–27.

Jaeschke, H., 2006. Mechanisms of liver Injury. II. Mechanisms of neutrophil-induced liver cell injury during hepatic ischemia–reperfusion and other acute inflammatory conditions. Am. J. Physiol. Gastrointest. Liver Physiol. 290, G1083–1088.

Kamal, S.A., 2009. Pathological studies on postvaccinal reactions of Rift Valley fever in goats. Virol. J. 6, 94.

Kolios, G., Valatas, V., Kouroumalis, E., 2006. Role of Kupffer cells in the pathogenesis of liver disease. World J. Gastroenterol. 12, 7413–7420.

Laughlin, L.W., Meegan, J.M., Strausbaugh, L.J., Morens, D.M., Watten, R.H., 1979. Epidemic Rift Valley fever in Egypt: observations of the spectrum of human illness. Trans. R. Soc. Trop. Med. Hyg. 73, 630–633.

Lewis, R.M., Cosgriff, T.M., Peters, C.J., Morrill, J.C., 1987. Differentiation of a human monocytic cell line associated with increased production of Rift Valley fever virus by infected cells. J. Med. Virol. 23, 207–215.

Madani, T.A., Al-Mazrou, Y.Y., Al-Jeffri, M.H., Mishkhas, A.A., Al-Rabeah, A.M., Turkistani, A.M., Al-Sayed, M.O., Abodahish, A.A., Khan, A.S., Ksiazek, T.G., Shobokshi, O., 2003. Rift Valley fever epidemic in Saudi Arabia: epidemiological, clinical, and laboratory characteristics. Clin. Infect. Dis. 37, 1084–1092.

McGavran, M.H., Easterday, B.C., 1963. Rift Valley Fever virus hepatitis: light and electron microscopic studies in the mouse. Am. J. Pathol. 42, 587–607.

McIntosh, B.M., Russell, D., dos Santos, I., Gear, J.H., 1980. Rift Valley fever in humans in South Africa. S. Afr. Med. J. 58, 803–806.

Meegan, J.M., Bailey, Charles, L., 1989. Rift Valley fever. In: Monath, T.P. (Ed.), The Arboviruses, Epidemiology and Ecology. CRC Press, Boca Raton, pp. 51–76.

Morrill, J.C., Jennings, G.B., Johnson, A.J., Cosgriff, T.M., Gibbs, P.H., Peters, C.J., 1990. Pathogenesis of Rift Valley fever in rhesus monkeys: role of interferon response. Arch. Virol. 110, 195–212.

Perkins, E.M., McCaffery, J.M., 2007. Conventional and immunoelectron microscopy of mitochondria. Methods Mol. Biol. 372, 467–483.
Sidwell, R.W., Smee, D.F., 2003. Viruses of the Bunya- and Togaviridae families: potential as bioterrorism agents and means of control. Antiviral Res. 57, 101–111.
Sitia, G., Iannacone, M., Aiolfi, R., Isogawa, M., van Rooijen, N., Scozzesi, C., Bianchi, M.E., von Andrian, U.H., Chisari, F.V., Guidotti, L.G., 2011. Kupffer cells hasten resolution of liver immunopathology in mouse models of viral hepatitis. PLoS Pathog. 7, e1002061.
Smith, D.R., Steele, K.E., Shamblin, J., Honko, A., Johnson, J., Reed, C., Kennedy, M., Chapman, J.L., Hensley, L.E., 2010. The pathogenesis of Rift Valley fever virus in the mouse model. Virology 407, 256–267.
Srichaikul, T., Nimmanitaya, S., Artchararit, N., Siriasawakul, T., Sungpeuk, P., 1977. Fibrinogen metabolism and disseminated intravascular coagulation in dengue hemorrhagic fever. Am. J. Trop. Med. Hyg. 26, 525–532.
Steele, K.E., Anderson, A.O., Mohamadzadeh, M., 2009. Fibroblastic reticular cells and their role in viral hemorrhagic fevers. Expert Rev. Anti Infect. Ther. 7, 423–435.
Struthers, J.K., Swanepoel, R., 1982. Identification of a major non-structural protein in the nuclei of Rift Valley fever virus-infected cells. J. Gen. Virol. 60, 381–384.
Swanepoel, R., Blackburn, N.K., 1977. Demonstration of nuclear immunofluorescence in Rift Valley fever infected cells. J. Gen. Virol. 34, 557–561.
Ursini-Siegel, J., Zhang, W., Altmeyer, A., Hatada, E.N., Do, R.K., Yagita, H., Chen-Kiang, S., 2002. TRAIL/Apo-2 ligand induces primary plasma cell apoptosis. J. Immunol. 169, 5505–5513.
Washburn, J.O., Lyons, E.H., Haas-Stapleton, E.J., Volkman, L.E., 1999. Multiple nucleocapsid packaging of *Autographa californica* nucleopolyhedrovirus accelerates the onset of systemic infection in *Trichoplusia ni*. J. Virol. 73, 411–416.
Yadani, F.Z., Kohl, A., Prehaud, C., Billecocq, A., Bouloy, M., 1999. The carboxy-terminal acidic domain of Rift Valley fever virus NSs protein is essential for the formation of filamentous structures but not for the nuclear localization of the protein. J. Virol. 73, 5018–5025.
Yamamoto, T., Kojima, T., Murata, M., Takano, K., Go, M., Chiba, H., Sawada, N., 2004. IL-1beta regulates expression of Cx32, occludin, and claudin-2 of rat hepatocytes via distinct signal transduction pathways. Exp. Cell Res. 299, 427–441.